Enhancement of EMAT's efficiency by using silicon steel laminations back-plate

Weiping Ren [1], Jianpeng He [2], Steve Dixon [3] and Ke Xu [1,*]

1 Collaborative Innovation Center of Steel Technology, University of Science and Technology Beijing, Beijing 100083, China; ping28198@126.com

2 National Engineering Research Center of Advanced Rolling Technology, University of Science and Technology Beijing, Beijing 100083, China; o832an@hotmail.com

3 Department of Physics, University of Warwick, Coventry CV4 7AL, UK; S.M.Dixon@warwick.ac.uk (S.D.)

* Correspondence: xuke@ustb.edu.cn; Tel.: +86-10-6233-2159

Abstract

Silicon steel laminations are introduced as the back-plate to an electromagnetic acoustic transducer (EMAT) to increase the efficiency of the EMAT by increasing the magnitude of the EMAT coil's dynamic magnetic field and the eddy current in the sample surface. A two-dimensional, non-linear finite element model is developed to quantify the effectiveness of the back-plate's different maximum permeability and saturation flux density, on increasing the eddy current density and the dynamic magnetic flux density in the specimen. A three-dimensional FE model is also developed, and confirms the expected result that the laminated structure of silicon steel (SiFe) markedly reduces the eddy current induced in the back-plate, when compared to a continuous slab of the steel. Experimental results show that silicon steel lamination can increase the efficiency of the EMAT in the cases both with and without a biasing magnetic field.

Key words

EMAT, Silicon steel lamination, back-plate, Lamb wave, non-linear finite element model

1, Introduction

Electromagnetic acoustic transducers (EMATs) are electromagnetically coupled ultrasonic transducers which are able to generate and detect ultrasonic waves on electrically conducting media. The EMAT's non-contact nature facilitates working at elevated temperature or on moving objects. The flexibility to easily change the shape of EMATs makes their application targets multifarious, from metal plates (strip), pipes, sticks to steel rails[1-3] . Furthermore, EMATs can generate various kinds of wave modes with different magnetic field and coil configurations, such as Rayleigh waves, Lamb wave, longitudinal waves, shear waves, torsional waves and others.

Compared with standard piezoelectric transducers, EMAT are usually orders of magnitude less efficient, leading to a relatively low sign-to-noise ratio (SNR). Various methods have been used to increase EMAT SNR, including various configurations of static magnetic fields [4,5,31], using soft magnetic alloys as a magnetic flux concentrator (MFC) [6] and coil geometries that enhance SNR by focusing the Rayleigh wave [7].

In this paper, laminated silicon steel is introduced as the back-plate to boost eddy current density and dynamic magnetic flux density in the specimen so as to enhance the efficiency of EMATs. A 2D non-linear finite element (FE) model is developed to study the relationship between magnetic properties of the back-plate material and both eddy current density and magnetic flux density in the specimen. A 3D FE model is also developed and the results reveal as expected, that

laminated structure of the silicon steel reduces equivalent conductivity dramatically, which is effective to suppress eddy current density in the back-plate. Two sets of experiments operated on the iron indicate the validity of the enhancement effect of silicon steel laminations to the efficiency of EMATs. This result is consistent with the findings of previous research that uses a non-conductive, high permeability magnetite back plate to enhance the EMAT efficiency [12]. In this paper, the key research question is if the benefit provided by high permeability of laminated steel structure outweighed the disadvantage of the eddy current losses when the coil is placed close to an electrical conductor.

2, Theory

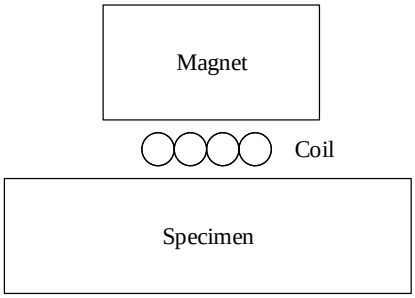

Fig. 1. A typical configuration of EMAT

A typical EMAT Configuration is shown in Fig. 1. The EMAT consists of a magnet, lacquered coils and specimen. A bulk magnet or electro-magnet is employed to provide vertical magnetic field. A narrowband tone burst or wideband pulse current is commonly used to excite the coil. Meander, spiral or racetrack coils are generally used to generate different type of ultrasonic waves [8]. The specimen is usually restricted to good conductor or some magnetic material. The Lorentz force, the magnetostriction force and the magnetization force are three mechanisms responsible for generating and receiving ultrasound in ferromagnetic material. In the non-magnetic materials, only the Lorentz force mechanism is presented[9]. It is now widely agreed that the Lorentz force is the largest transduction mechanism on steel materials, regardless of the level of magnetic bias field employed [10], and this mechanism will be the focus in this paper.

An eddy current $\boldsymbol{J}_e$ is excited in the metal specimen when time varying current flows in the coil which is close to the metal specimen, and a dynamic magnetic field $\boldsymbol{B}_d$ is also produced. The dynamic Lorentz force $\boldsymbol{F}_d$ and the static Lorentz force $\boldsymbol{F}_s$ are produced by the eddy current under the interaction with dynamic magnetic field and external static magnetic field [11]. The $\boldsymbol{F}_d$ and $\boldsymbol{F}_s$ are given respectively by,

$$\boldsymbol{F}_s = \boldsymbol{J}_e \times \boldsymbol{B}_s \tag{1}$$

$$\boldsymbol{F}_d = \boldsymbol{J}_e \times \boldsymbol{B}_d \tag{2}$$

where $\boldsymbol{B}_s$ is the magnetic flux density from static magnetic field, $\boldsymbol{B}_d$ is the magnetic flux density from dynamic magnetic field. The total Lorentz force is,

$$\boldsymbol{F} = \boldsymbol{F}_s + \boldsymbol{F}_d \tag{3}$$

the dynamic magnetic field $\boldsymbol{B}_d$ is given in terms of the magnetic vector potential $\boldsymbol{A}$ as,

$$\boldsymbol{B}_d = \nabla \times \boldsymbol{A} \tag{4}$$

and the eddy current in the metal sample is given by,

$$\boldsymbol{J}_e = -\sigma \frac{\partial \boldsymbol{A}}{\partial t} \tag{5}$$

where σ is the electrical conductivity of the specimen.

Equations (1-5) show how the Lorentz force $\boldsymbol{F}$ is related to $\boldsymbol{B}_s$, $\boldsymbol{B}_d$ and $\boldsymbol{J}_e$. The magnitude of $\boldsymbol{F}_s$ is proportional to the magnitudes of $\boldsymbol{B}_s$ and $\boldsymbol{J}_e$, and the magnitude of $\boldsymbol{F}_d$ is proportional to the magnitudes of $\boldsymbol{B}_d$ and $\boldsymbol{J}_e$. It is clear that increasing the dynamic magnetic field $\boldsymbol{B}_d$ and consequently the eddy current $\boldsymbol{J}_e$ will increase the size of the Lorentz force.

To increase the efficiency of an EMAT's energy conversion, a back-plate is added to the configuration of EMAT as shown in Fig. 2. Soft magnetic materials usually act as the material of the back-plate. Earlier work used a 2-D FE model using COMSOL to explain how the presence of a high permeability ferrimagnetic back plate could enhance the eddy current of an EMAT coil due to magnetization of the backplate and produce a corresponding increment in coil inductance [12]. In this paper, a 2-D, non-linear FE model is developed to simulate the contribution of the back-plate with different electromagnetic properties to $\boldsymbol{B}_d$ and $\boldsymbol{J}_e$ in the specimen, the model will be introduced in next section.

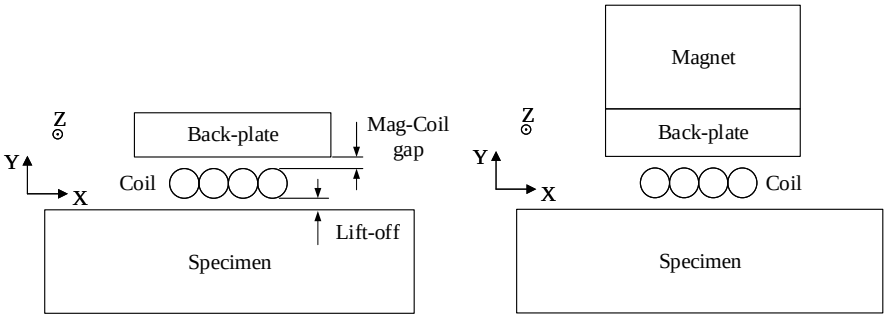

a) b)

Fig. 2 Two configurations of the EMATs with the back-plate, a) Without a bias magnetic field, b) With a bias magnetic field.

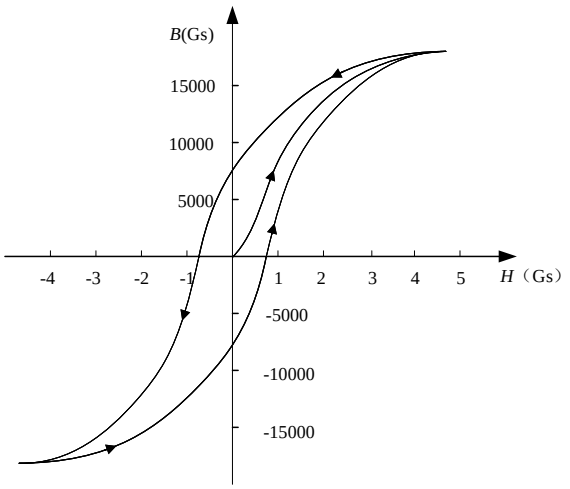

Fig. 3 A typical magnetization and hysteresis curve for soft iron (Gauss system of units)

Iron, iron alloys, nickel, nickel alloys, etc. are usually called ferromagnetic materials which are non-linear materials considering their magnetization process. The magnetization process can be described as:

$$B = \mu_0(H + M) \tag{6}$$

where H is magnetic field intensity, M is magnetization, μ_0 is the permeability of free space and B is magnetic flux density. There is no direct relation between M and B for a ferromagnetic material. The magnetization M depends on the whole past history of materials, and not only on the value of B. The relation between H and B can be obtained from experimental measurements. A typical magnetization and hysteresis curve for soft iron is shown in Fig. 3 which is usually called BH curve[13]. The figure shows the relation between B and H in soft iron; initially, it takes only a relatively small H to make a large B. At higher values of H, the magnetization curve levels off, indicating the saturation of the iron. With the scales of the figure, the curve appears to become horizontal. But it continues to rise slightly for larger fields, when B becomes proportional to H, and with a unit slope. That's reason why this type of materials is called nonlinear material. When the magnetization process is operated in a relative small range of magnetic field intensity, the relationship between B and H can be approximated by an equation as:

$$B = \mu_0\mu_r H \tag{7}$$

where μ_r is relative permeability. The maximum relative permeability (μ_{max}) and the saturation flux density (B_s) are usually introduced to describe the magnetic features of soft magnetic materials. For example, μ_{max} for silicon steel (3% Si, 97% Fe) is about 7000 and B_s is about 2.0 T, whilst μ_{max} for Mn-Zn ferrite PC40 (TDK, Japan) is about 4100 and B_s is about 0.5 T [14]. Conversely, the magnetization curve can be fitted carefully using μ_{max} and B_s according to the typical features of BH curve. In this paper, 54 magnetization curves are fitted with the values of μ_{max} and B_s from Table 1. These curves represent different characteristics of magnetic materials which are employed to simulate the magnetization process of them in the next section.

Table 1, the values of μ_{max} and B_s used to fit the magnetization curve

	Values								
B_s(T)	0.05	0.1	0.2	0.5	1	2	-	-	-
μ_{max}	5	10	20	50	70	100	500	1000	5000

3，Simulation analysis

3.1 Eddy current and dynamic magnetic field in specimen

To quantify the relationship between magnetic properties of back-plate and eddy current density in the specimen, a non-linear 2-D FE model is developed using COMSOL Multiphysics 5.2®, and magnetic field (mf) component from the AC/DC module is employed in the simulation. A linear coil is applied in the model, and can analyze the process in a 2-D model, ignoring the effects of z direction. The model consists of back-plate domain, coils domain, specimen domain and air domain as showed in Fig. 4. The width of back-plate domain W_b=20 mm and the height H_b=10 mm. The diameter of the coil is 0.68 mm, and the gap between back-plate and coil, the gap

between coil and specimen are both 0.2 mm. The height of specimen H_{sp}=10 mm, and the width of the whole model W=25 mm, height H=26 mm. A bias magnetic field is usually utilized in EMAT generator design but not always necessary [15] (although it is required for an EMAT to operate as a detector). Moreover, eddy current and dynamic magnetic field in the specimen are the main concerns, so bias magnetic field is ignored in our simulation. In order to get a more precise simulation result, a non-linear equation is employed as the constitutive equation in the back-plate domain and the specimen domain,

$$\mathbf{H} = f(|\boldsymbol{B}|)\frac{\boldsymbol{B}}{|\boldsymbol{B}|} \tag{8}$$

where the function f maps the magnitude of $\boldsymbol{B}$ to magnitude of $\mathbf{H}$, and the functional relation is obtained from the BH curve. The BH curves of the back-plate domain are fitted by the values in table 1. The low carbon steel 1020 acts as the specimen whose BH curve comes from the in-built material library of COMSOL. The electrical conductivity, σ , of the back-plate is limited to 5×10^{-5} S/m to indicate an insulator. The σ of the specimen is set to 8.41×10^{6} S/m, and the σ and μ_r of the coils are 5.998×10^{7} S/m and 1 respectively. A pulse of current is applied to excite the coil as shown in Fig. 5. The current signal is featured with a peak of approximately 270 A and a time range of 0-10 μs. The magnetic insulation boundary condition is applied to the boundaries of the whole model to assume the infinite dimension of the air and the specimen. The grid size near the coil is set to 0.01 mm (equals to electro-magnetic skin depth) in the back-plate domain and the specimen domain to insure the accuracy of the simulation result. MUMPS (Multifrontal Massively Parallel Sparse Direct Solver) is selected to solve the model, and the automatic highly nonlinear(Newton) method is chosen as the nonlinear method.

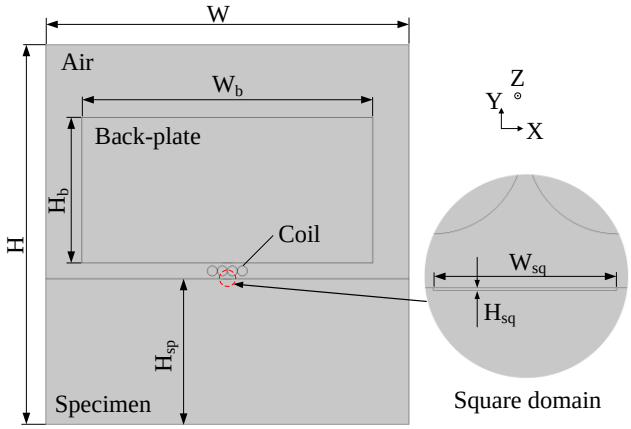

Fig. 4 The schematic of the 2-D model.

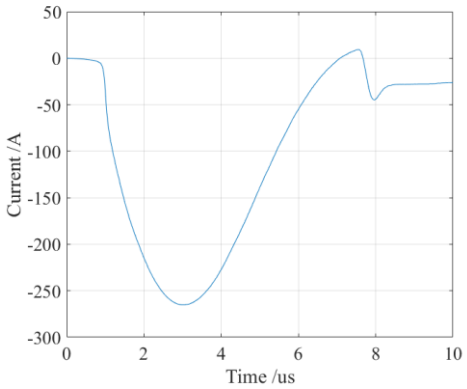

Fig. 5 The excitation current used in the simulation which is sampled from the EMAT transmitter by using a 0.1 Ω resistor in series with the induct wire.

To measure eddy current density and magnetic field in the specimen conveniently, a small square domain is set up just below the coil in the specimen domain, with the width W_{sq} = 0.68 mm and the height H_{sq} = 0.01 mm (see Fig. 4). The top of the square coincides with that of the specimen domain. The electromagnetic interaction volume of EMATs is restricted to a shallow surface layer which is limited by the electro-magnetic skin depth [16]. The height of the square domain equals the skin depth calculated from the present configuration. The averages of the x component of magnetic flux density $\boldsymbol{B}_x$ and the z component of eddy current density $\boldsymbol{J}_z$ in the square domain are calculated, and the values are recorded at each interval time 0.1 μs.

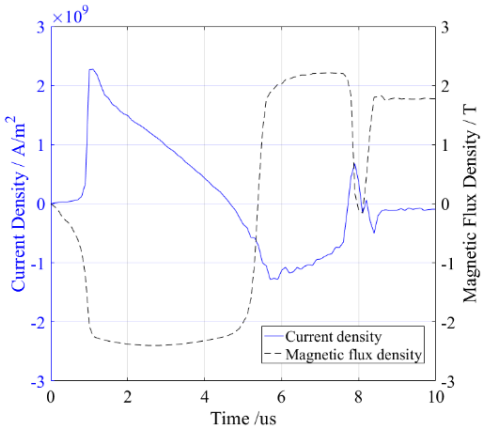

Fig. 6 Eddy current density and magnetic flux density in specimen.

Time-varying curves of $\boldsymbol{B}_x$ and $\boldsymbol{J}_z$ are plotted in Fig. 6. The data source is from the simulation result where $\mu_r = 1$ for the back-plate. The current density rises sharply at the time of 1μs, and then descends slowly. The direction alters at 4.6 μs. Some authors argue that the eddy current is a mirror image of the coil current and flows in the opposite direction [10,16]. Obviously, the simulation result is inconsistent with these arguments. The eddy current density is approximately proportional to the derivative of the excitation current in the coil, merely with a phase difference, which can be also deduced from equations (4-5). This has been explained in more detail by other workers [17].

To investigate the behaviour of $\boldsymbol{J}_z$ under different parameter values for μ_{max} and $\boldsymbol{B}_s$ of the back-plate, the average value of $\boldsymbol{J}_z$ in the time range from 2 μs to 4 μs are calculated, and

$\boldsymbol{B}_x$ is also processed in the same way. To avoid confusion, the symbols μ_{max} and $\boldsymbol{B}_s$ represent the maximum permeability and saturation permeability of the back-plate domain respectively, the symbols $\boldsymbol{J}_z$ and $\boldsymbol{B}_x$ indicate the z component of eddy current density and the x component of magnetic flux density in the small square domain respectively. The curves of $\boldsymbol{J}_z$ varying with μ_{max} and $\boldsymbol{B}_s$ are shown in Fig. 7a, whilst $\boldsymbol{B}_x$ is shown in Fig. 7b. The results of Fig. 7a reveal that $\boldsymbol{J}_z$ increases with μ_{max} when the μ_{max} < 100, but the gradient of $\boldsymbol{J}_z$ becomes much smaller when μ_{max} > 100. As expected, $\boldsymbol{J}_z$ increases with $\boldsymbol{B}_s$ for values of $\boldsymbol{B}_s$ < 0.2 T, whilst the change of $\boldsymbol{J}_z$ is insignificant with increasing $\boldsymbol{B}_s$ for values of $\boldsymbol{B}_s$ > 0.2 T. Unsurprisingly, the behaviour of $\boldsymbol{J}_z$ is comparable to that of $\boldsymbol{B}_x$, as is clear in Fig. 7b. The values for $\boldsymbol{J}_z$ and $\boldsymbol{B}_x$ are 1.024×10^9 A/m and -2.378 T respectively when μ_r of the magnetic back-plate is set to 1. Once $\boldsymbol{B}_s$ is larger than 0.2T and μ_{max} is greater than 100, both $\boldsymbol{J}_z$ and $\boldsymbol{B}_x$ become stable with gradients of 25% and 3.9% respectively. This non-linear relation between the relative permeability of the back-plate and the magnetic flux density in the specimen is described in the discussion section.

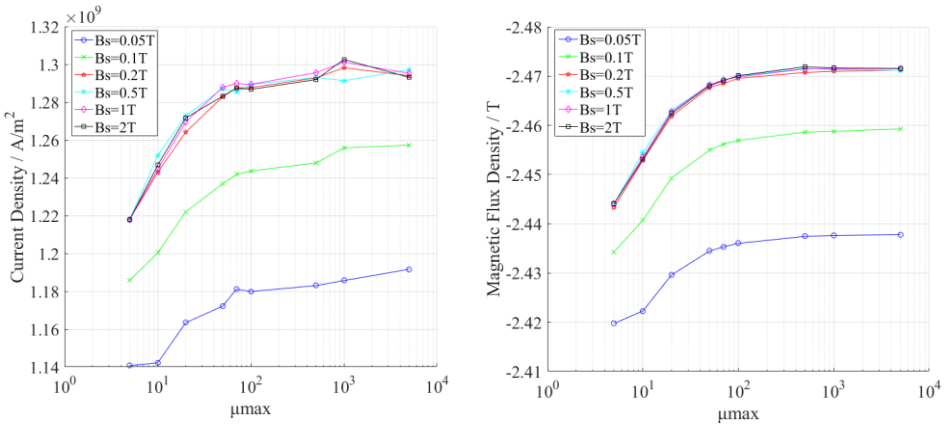

a) b)

Fig. 7 Current density and magnetic flux density in the square domain varying with the μ_{max} and the $\boldsymbol{B}_s$ of the back-plate. a) the current density $\boldsymbol{J}_z$ in the small square domain, b) the magnetic flux density in the small square domain.

The previous conclusions are based on the hypothesis that the back-plate has a low electrical conductivity, which is obviously not accurate for steel or iron. Therefore, $\boldsymbol{J}_z$ and $\boldsymbol{B}_x$ are also simulated with varying electrical conductivity of the back-plate, σ_m. In the simulation, the BH curve is obtained from the built-in values for silicon steel (35PN360 in COMSOL). The silicon steel tested in our experiments, has μ_{max} and $\boldsymbol{B}_s$ of approximately 7000 and 2 T respectively. The results of $\boldsymbol{J}_z$ and $\boldsymbol{B}_x$ are calculated and plotted in Fig. 8, revealing that there is a sharp decline in the values of both $\boldsymbol{J}_z$ and $\boldsymbol{B}_x$ when $\sigma_m > 1 \times 10^5$ S/m. The eddy current density in the back-plate is also shown in Fig. 8. The simulation results show that as expected, the eddy current in back-plate has an adverse impact on the generation of the eddy current in the specimen.

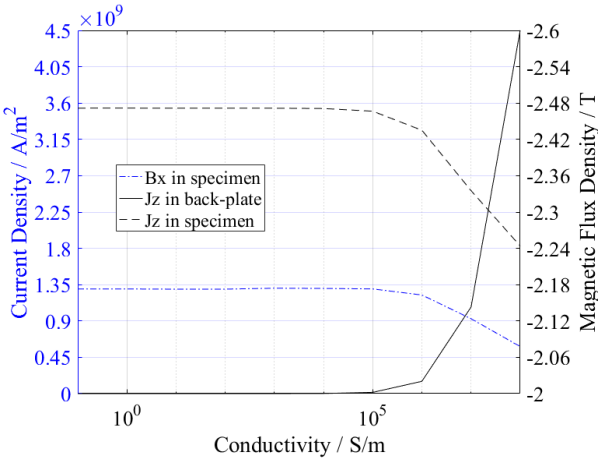

Fig. 8 Current density, magnetic flux density in the specimen and the current density in the back-plate varying by the conductivity of back-plate.

3.2 Eddy current in laminations

In the previous section, it is concluded that there is an impressive enhancement of the $\boldsymbol{J}_z$ and $\boldsymbol{B}_x$ when the μ_{max} and $\boldsymbol{B}_s$ of the back-plate are greater than 100 and 0.2 T respectively, and the conductivity is less than 1×10^5 S/m simultaneously. Fortunately, there are a number of materials meeting these requirements such as Mn-Zn ferrite, Ni-Zn ferrite and amorphous materials [14,18]. However, almost all of these materials have disadvantages such as lower saturation flux density (<0.65T) and lower Curie temperature (<300℃). To a large extent, these weaknesses restrict the application of the back-plate to the EMATs in many situations. For instance, they are hardly used as the core of electromagnet or at elevated temperatures. Materials with higher saturation flux density and higher Curie temperature usually accompany with higher conductivity such as silicon steel (SiFe) and Fe-Co-V. In practical application, the SiFe is commonly processed into the laminations which are widely used in transformers and electric motors. Laminated structure of silicon steel can memorably reduce eddy-current loss and hysteresis loss in the applications of transformers[14]. In this paper, SiFe laminations are introduced in EMATs to reduce the adverse effect of high conductivity of them without affecting the features of high saturation flux density and Curie temperature.

A 3D FE model is developed to analyze eddy current distribution in the SiFe laminations when they are employed as the back-plate of EMATs. As a contrast, the distribution in a same size SiFe block is also simulated. Both two geometric models are shown in Fig. 9, in which electrical conductivity of the SiFe is 1.85×10^6 S/m, meanwhile, the relative permittivity and relative permeability are 1 and 7000 respectively. For the repeated arrangement of the laminations, only 4 slices of SiFe sheets are considered in the model. The thickness of a single lamination is set to 0.35 mm, and the height is 3 mm, width is 3 mm. The SiFe block has the same size with the laminations. The thickness of the air-gap between two SiFe slices in the laminations is set to 5 um to replace the dielectric film. The diameter of the coil used in the model is 0.68 mm, and the gap between the back-plate and the coil is 0.2 mm. The driving current through the coil is the same with that implemented in the 2-D model above. One-half of the model is set up using mirror symmetry to generate the entire model and speed up calculation time. Actually, more attention goes to the comparison of eddy currents in the block and the laminations, rather than their specific

value, so a linear model is applied in the 3-D model to make the calculation easier to converge which can also achieve relatively accurate results.

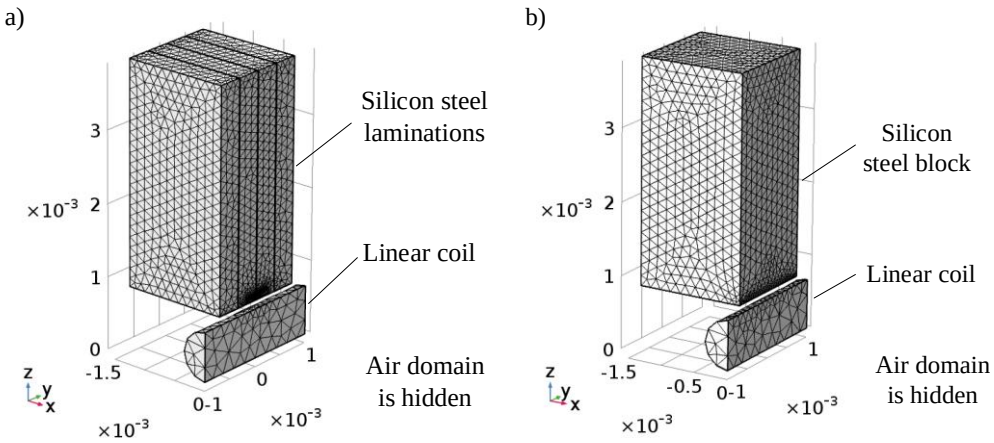

Fig. 9 the 3D model of laminations and block, the unit of the values is meter. The model of silicon steel laminations, b) the model of silicon steel block.

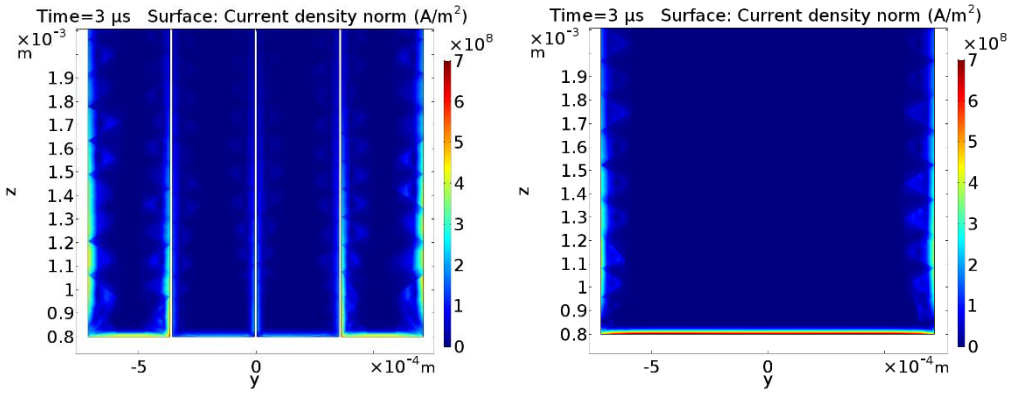

a) b)

Fig. 10 The eddy current distribution in the laminations and the block. a) in the laminations, b) in the block.

The sectional drawings of the current density distribution in the laminations and the block are shown in Fig. 10. The data sets are acquired synchronously at 3 µs. The cross section is parallel to y-z plane and the value of x is 0 mm. The current density distribution is obviously different between the laminations and the block. In the laminations, the eddy current density in inner layers is obviously less than external layers and the distribution of the eddy current density in the block is stable in y-direction. The average eddy current density in the skin layer of both the inner laminations and the block are calculated. The eddy current densities in the laminations and the block are 1.4×10^8 A/m^2 and 6.5×10^8 A/m^2 respectively. Considering the inverse relationship between current density and the conductivity, the laminated structure reduces the y-direction equivalent conductivity of the SiFe from 1.85×10^6 S/m to 4.5×10^5 S/m. The decrease of the equivalent conductivity of laminated SiFe makes it a viable choice for the back-plate of an EMAT transmitter coil.

4, Experiment validation

In order to verify the effectiveness of the SiFe laminations as EMAT back-plates, two groups of experiments are implemented. The first group is operated without bias magnetic field, and the second utilizes a vertical bias magnetic field.

The configuration of the EMAT transmitter (without magnetic field) is shown in Fig. 11. A racetrack coil of 4 turns of lacquered copper wire is used as the EMAT generation coil. The SiFe laminations B35A360 (Baoshan Iron & Steel Co., China) are placed closely behind the coil, with the surface of the laminations perpendicular to the length direction of the coil. The thickness of each lamination is 0.35 mm. A 1 mm low carbon steel plate acts as the specimen. The steel plate and the coil are isolated by a 0.2 mm plastic plate as the air-gap. Likewise, another same plastic plate is inserted into the gap between the coil and the laminations. In the comparative experiments, SiFe laminations are replaced by a piece of acrylonitrile butadiene styrene(ABS) plastic, a same size low carbon steel (C 0.2%) and Mn-Zn ferrite PC40 respectively. The electromagnetism characteristics of the ABS plastic are similar to the air, which represents the case with no back-plate.

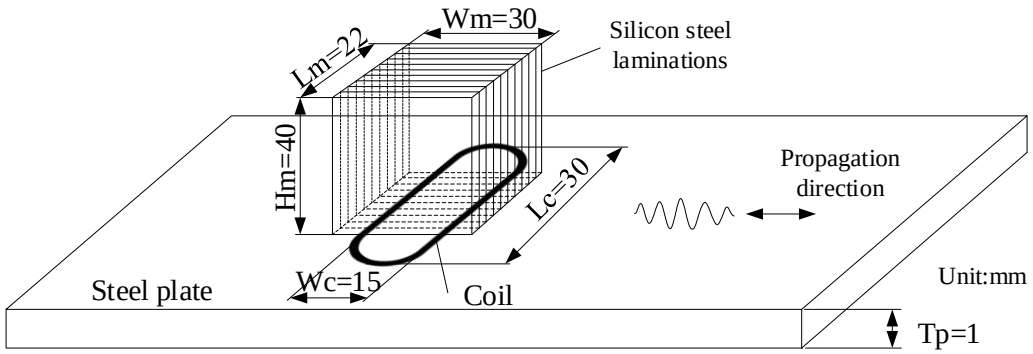

Fig. 11 The configuration of EMAT transmitter (without the magnet)

In the next experiments, bias magnetic field is provided by two NdFeB magnets, which are shown in Fig. 12. In order to obtain a relatively homogeneous vertical magnetic field, two magnets are employed on opposite sides of the plate orientated with the same magnetic polarity direction. The bias magnetic field near the coil is kept at the equivalent value of 0.38 T by adjusting the distance between the back-plate and the magnet or the distance between the steel plate and the magnet (without back-plate) in all experiments. A gauss meter is employed to measure the magnetic flux density at the test point shown in the Fig. 12. Similarly, the back-plate is replaced by SiFe, Mn-Zn ferrite and low carbon steel respectively in the actual experiments.

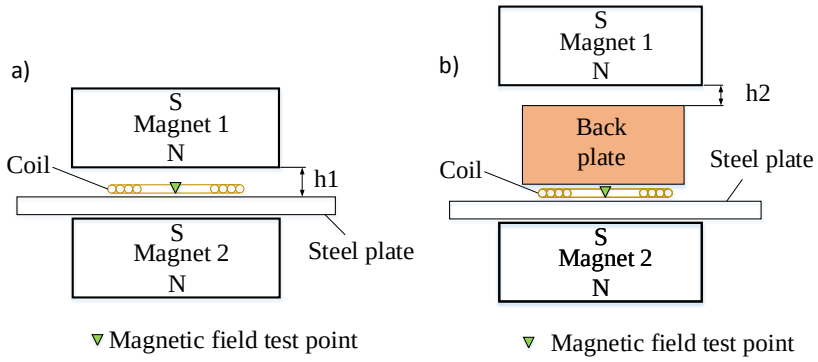

Fig. 12 The configuration of EMAT transmitter (with bias magnetic field), a) without back-plate, b)

with the back-plate. The magnetic field test point is at the center of the coil. The distance h1 and h2 is adjustable.

The intensity of ultrasonic wave generated by the EMAT becomes larger with the boost of the amplitude of the current in the coil[19], whilst the excitation current depends on the impedance matching between the coil and the power source[20,21]. The magnetic reluctance around the coil is reduced due to the magnetic back-plate, which leads to an increment of the coil's inductance. Therefore, the excitation current is also measured with the different back-plates, and is shown in Fig. 13. The peak value of the current is approximately 250 A with several microseconds duration and the peak voltage is about 800V. There is minor difference of the current between the Mn-Zn ferrite back-plate and the case without back-plate. The SiFe laminations and the low carbon steel have a similar influence on the excitation current, and the peak value of the current is 98% of that measured without a back-plate.

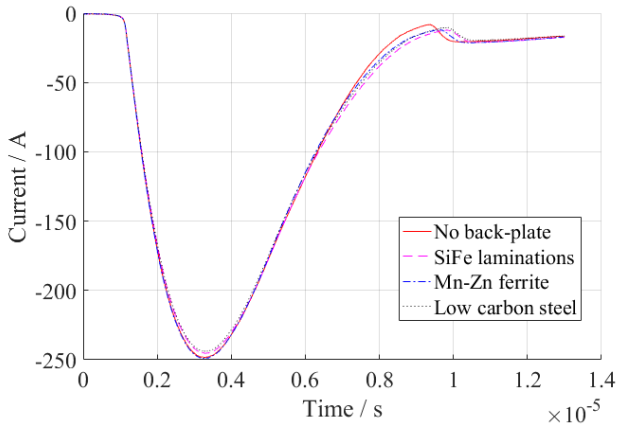

Fig. 13 Excitation current flowing through the coil, measured with no back-plate, SiFe laminations, Mn-Zn ferrite and low carbon steel. A 0.1 Ω resister is connected in series with the coil to measure the current.

Lamb waves and shear horizontal (SH) waves are two types of ultrasonic wave modes excited by the EMAT in the plate[22]. The EMAT configuration in our experiments can generate multimode Lamb waves, which are separated into two groups of modes, symmetric (S) and anti-symmetric (A), that have complex but well understood dispersion curves [23]. The S0 mode and A0 mode Lamb waves are generated in the experiments as we are operating at a relatively low frequency thickness product, below the cut-off of higher order modes. A traditional lamb wave EMAT receiver equipped with a vertical magnet and linear coils is applied to receive the ultrasonic wave at a position 150 mm apart from the transmitter.

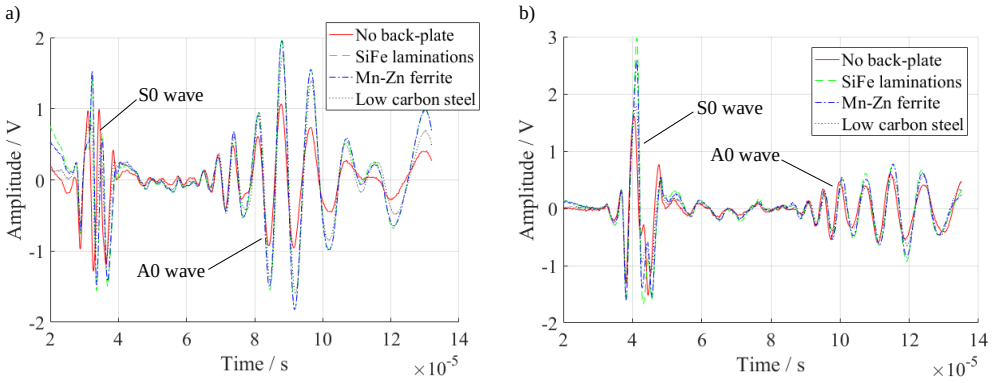

Fig. 14 Received Lamb wave signal, a) without bias magnetic field, b) with the bias magnetic field. The wave packet with a higher frequency and reaching earlier is S0 wave, and the other packet is A0 wave

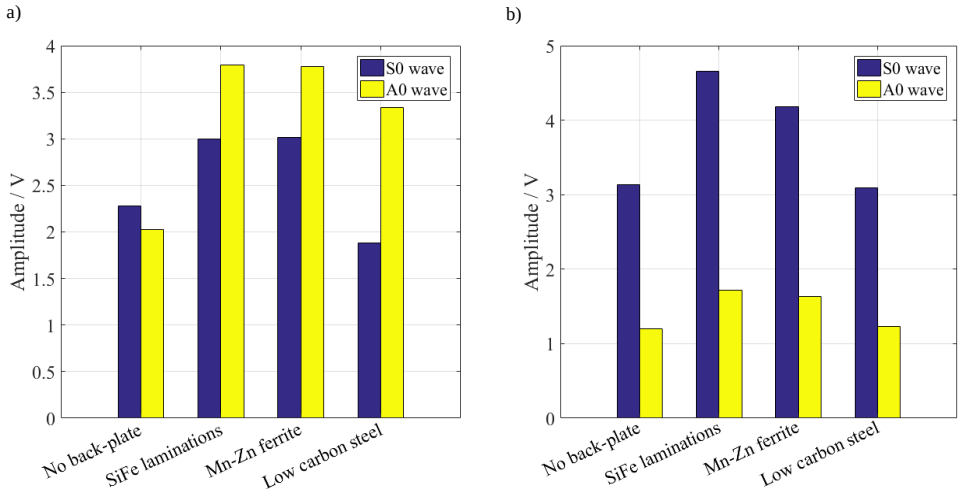

Fig. 15 Peak to peak values of S0 and A0 wave with the different back-plates, a) without the bias magnetic field, b) with the bias magnetic field.

Fig. 14 shows the received Lamb waves under different back-plates conditions used in the experiments. To conveniently contrast the amplitude of these waves, the peak-to-peak value of S0 wave and A0 wave are calculated and shown as bar chart in Fig. 15. In the first group, SiFe laminations and Mn-Zn ferrite both enhance the amplitude of A0 wave for about 86%, whilst 31% for S0 wave. Whereas, the low carbon steel has a less contribution and sometime even restraints the S0 wave due to its more higher conductivity. However, the contribution of SiFe laminations becomes more significant than that of Mn-Zn ferrite when the vertical bias magnetic field is provided. The former can improve A0 wave and S0 wave for about 43% and 48% respectively, while the later can only reach 35% and 33%. In addition, the low carbon steel back-plate has almost no contribution to the enhancement of Lamb waves.

5, Discussion

The experiment results validate that soft magnetic material back-plate can significantly improve the efficiency of the EMAT whether there exists bias magnetic field. It is because soft magnetic material back-plate enhances dynamic magnetic field and eddy current density in the specimen, which is supported by the numerical simulation results. In the conventional EMATs, a

permanent magnet (hard magnetic material) is usually used to provide bias magnetic field, whereas, it always comes with higher coercivity. For example, the coercivity of NdFeB grade N38 (used in experiments) is 920 kA/m at 20°C (Eclipse Magnetics Limited, UK), which is much higher than the 160 kA/m magnetic field strength generated by EMAT coil (from the simulation). It indicates that the NdFeB cannot be magnetized or demagnetized by the EMAT coil. Therefore, the permanent magnet is just equivalent to the free space for the exciting coil.

Under the vertical distribution of the bias magnetic field, the distribution of the static bias magnetic field is bound to change due to the introduction of the magnetic back-plate. Therefore, the influence of such changes on the EMAT's efficiency needs to be further evaluated. A 2D finite element model is established in this paper to simulate the distribution of static magnetic field in the sample when the back-plate has different heights and widths. Fig. 16 shows the distribution of the magnetic flux density when the height of the back-plate = 1 mm, the width = 20 mm and the width of magnet = 30 mm. The residual flux density of the magnet in this model is set to 1.21 T (NdFeB grade N38), the material of the back-plate is SiFe, and the coil is omitted. The distribution of magnetic flux density in the simulation results shows that the distribution of static magnetic field in the steel plate is particularly inhomogeneous. The magnetic flux density near the edges on both sides of the magnet is larger and the middle is lower relatively. This nonuniformity is higher than the results when the sample is aluminum [5]. The magnetic flux density distribution near upper surface in the specimen is plotted as a curve, as shown in Fig. 17. Fig. 17a shows that the intensity of magnetic flux density decreases as the height of the back-plate increases, and this increment becomes obscure when the height is less than 1 mm. As can be seen from Fig. 17b, the inhomogeneity of the magnetic flux density in the sample becomes more noticeable when the width of the back plate is greater than or equal to that of the magnet. Therefore, it is recommended that the height of the back-plate is limited to 1 mm and the width is smaller than that of the magnet.

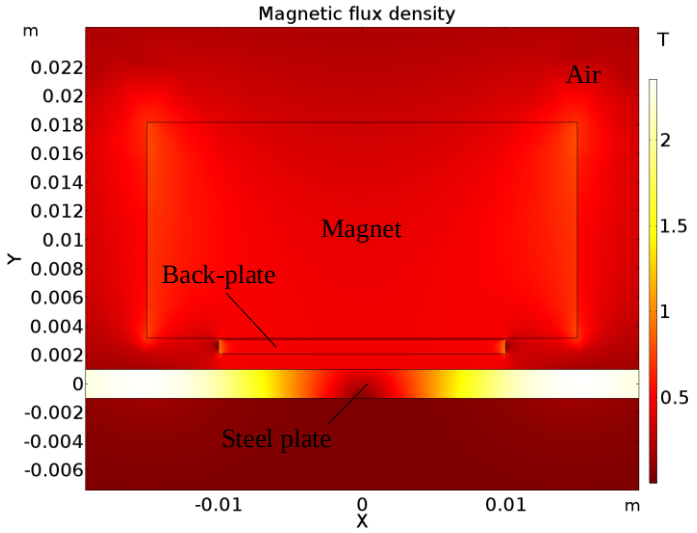

Fig. 16 The magnetic flux density distribution when back-plate width = 20 mm, height =1 mm

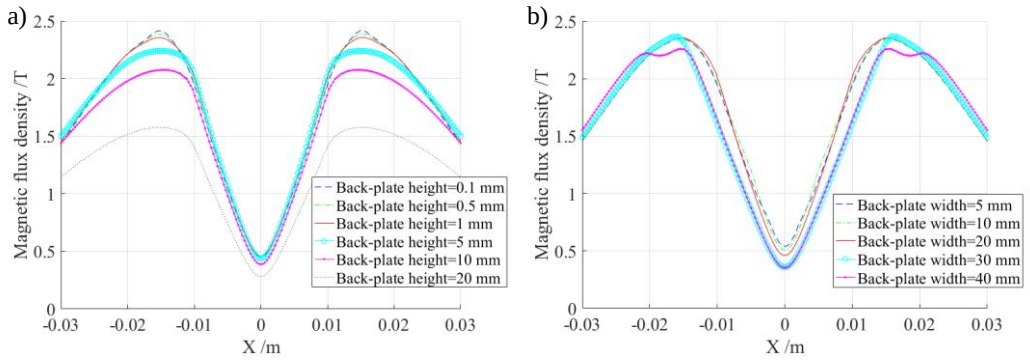

Fig. 17 The magnetic flux density distribution near the surface in the specimen (0.01 mm under the surface), a) varying with height of back-plate when width = 20 mm, b) varying with width of back-plate when height = 1 mm; X axis is the horizontal position and the zero indicates the center of the specimen.

This paper has mainly studied the influence of back-plate's electromagnetic parameters on the eddy current and dynamic magnetic field in the samples, but, whether the size of the back-plate would affect them also needs to be further discussed. Therefore 2-D FE model with different heights of back-plate is also developed. The magnetic field flux density and current density in the sample are detected and shown in Fig. 18. The results show that they are suppressed when the thickness of the back-plate is less than 0.5 mm. Hence, the recommended minimum thickness of the back-plate is 0.5mm.

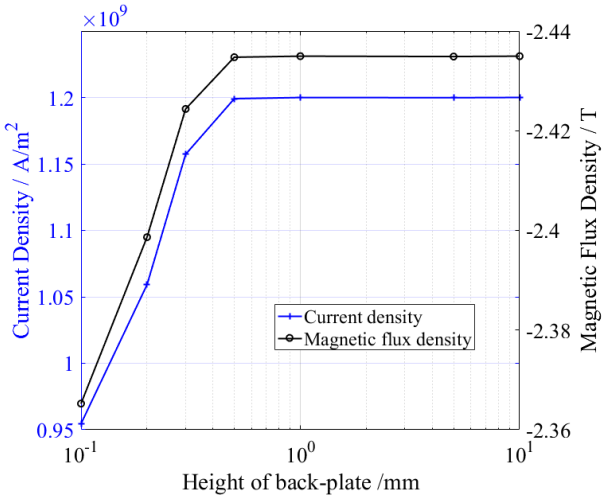

Fig. 18 Current density and magnetic flux density in specimen varying with the height of back-plate

The numerical and experimental results lead to the conclusion that magnetic back-plate with higher relative permeability can enhance magnetic flux density in the specimen. Moreover, there is a nonlinear relationship between μ_r of back-plate and the magnitude of B. This phenomenon can be explicated by the Maxwell electromagnetic equations:

$$\oint_l H \cdot dl = \int_s J_c \cdot ds \tag{9}$$

where l is a closed curve as the dashed showed in the Fig. 19, s is the surface bounded by l and J_c is current density in the coil. It is assumed that there is no eddy current in the back-plate and the eddy current in the specimen is ignored as well. The curve l is divided into 4 sections by the discontinuous interface, so the equation could be rewritten as:

$$\sum_{i=1}^{4} \int_{l_i} H_i \cdot ds = \int_s J_c \cdot ds \tag{10}$$

Considering a point at the bottom boundary of the back-plate, y component of magnetic flux density B_y in the back-plate equals to B_y in the air. For the continuity of B_y,

$$\mu_0 \mu_r H_{ym} = \mu_0 H_{yair} \tag{11}$$

where H_{ym} and H_{yair} are y components of magnetic field strength near the interface in the back-plate and the air respectively. H_{ym} attenuates proportionally with the growth of the μ_r of the back-plate. H has a sudden change at the interface between the back-plate and the air. Thus, it can be qualitatively confirmed that H_4 reduces when μ_r rises, meanwhile, H_1, H_2 and H_3 would increase for the identical J_c. However, the increments of H_1, H_2 and H_3 become ignorable when $H_3 \gg H_4$.

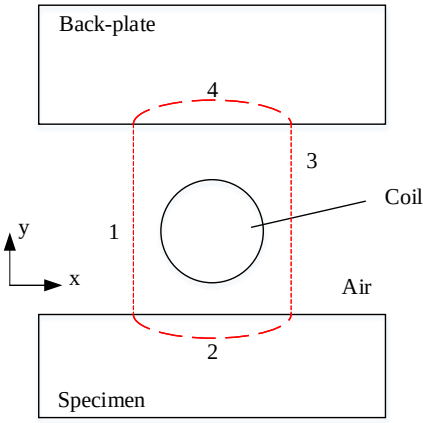

Fig. 19 the magnetic circuit in the back-plate and the specimen around the coil. The dash line is the magnetic path which is divided into 4 sections as the number signed.

The experiments results show that SiFe laminations and Mn-Zn ferrite have similar impact on the Lamb waves when bias magnetic field is not provided. However, there is an unequal growth rate between S0 wave and A0 wave with the rate of 32% and 87% respectively. It is usually considered that S0 wave is mainly generated by in-plane force such as the force dominated by the equation (1) and the magnetostriction force caused by dynamic magnetic field, and A0 wave is mainly generated by out-plate force which is dominated by the equation (2). Certainly, both in-plane and out-plane force contribute to S0 and A0 waves [25,26] . As a result, it can be deduced that A0 wave will rise with the boost of both $\boldsymbol{J}_e$ and $\boldsymbol{B}_d$, whereas S0 wave increase mainly with $\boldsymbol{B}_d$ when there is no bias magnetic field. Therefore, the increment rates of S0 and A0 wave are different. Fig. 15b shows that the enhancement for Lamb waves is different in using SiFe laminations and Mn-Zn ferrite back-plates if vertical bias magnetic field exists. A possible explanation is that the superposition of $\boldsymbol{B}_d$ and $\boldsymbol{B}_s$ makes the magnetic field of Mn-Zn ferrite saturated due to its lower saturation flux density of 0.5T. So, SiFe laminations has a better performance when vertical bias magnetic field is provided.

Relative magnetic permeability μ_r of soft magnetic materials is frequency dependent[27,28]. Generally, μ_r decreases with the frequency, which could be obtained from experimental measurements[29], or through calculation[30]. The simulation results above do not consider the effect of operation frequency, so the μ_r of the back-plate should be transformed to the value at the corresponding frequency in practical applications. The equivalent conductivity of the laminations is relative to the thickness of single lamination. Thinner laminations usually lead to a

lower equivalent conductivity. However, they also bring about a lower equivalent permeability since constant thickness of the dielectric film between the laminations. Additional experiments (not shown) indicate that both 0.5 mm and 0.35 mm thick laminations can achieve almost the same enhancement to the amplitude of lamb waves. Since the orthogonality between lamination's main surface and coil's tangent line is required, the arrangement of the laminations would become a bit complicated when the shape of the coils is anomalous. The priority of SiFe laminations is that they are accompanied with both higher saturation flux density (2.0T) and Curie temperature (750°C), which leads to wider applications. Furthermore, the feature of higher saturation flux density makes it possible to be used as magnetic core of electromagnet and the back-plate of the EMAT if the bias magnetic field is provided by an electromagnet. Another method is raised to enhance the strength of static bias magnetic field by adding a ferromagnetic core into several face-to-face magnets [31]. Further research could enhance the efficiency of the EMATs by combining this method with adding back-plate.

6, Conclusions

In this paper, A 2D nonlinear finite element model is developed to study the variation of both magnetic flux density and eddy current density in the specimen with different magnetic properties of the back-plate. The numeric simulation suggests that both magnetic flux density and eddy current density in the specimen are enhanced with the increment of back-plate's relative permeability and saturation flux density. Moreover, the eddy current density and the magnetic flux density increase 25% and 3.9% respectively when the back-plate's relative permeability and saturation flux density are boosted from 0 to 100 and 0.2 T separately. However, these improvements will decline with the rise of back-plate's electrical conductivity. Furthermore, it is recommended to set the height of the back-plate to 1mm and the width to be less than that of the magnet.

A 3D finite element model is also developed to reveal the utility of laminated SiFe in reducing the eddy current in the SiFe when it is used as the back-plate of EMAT. The laminations assembled with 0.35 mm thick SiFe sheets can reduce equivalent conductivity of SiFe from 1.85×10^6 S/m to 4.5×10^5 S/m. The decline of the conductivity makes it possible to be used as the back-plate of the EMAT.

Two sets of experiments are carried out to validate that SiFe laminations acting as the back-plate can enhance excitation efficiency of the transmitter significantly both with and without bias magnetic field. The result also reveals that both A0 waves and S0 waves of Lamb waves are promoted for different extents. These results are supported by the numeric simulation. SiFe laminations perform better than Mn-Zn ferrite when vertical bias magnetic field is provided. Additionally, higher Curie temperature of SiFe makes it possible to be used in the elevated temperature application.

References

1. Petcher, P.A.; Potter, M.D.G.; Dixon, S. A new electromagnetic acoustic transducer (EMAT) design for operation on rail. *NDT&E Int* **2014**, *65*, 1-7.
2. Seung, H.M.; Park, C.I.; Kim, Y.Y. An omnidirectional shear-horizontal guided wave EMAT for a metallic plate. *Ultrasonics* **2016**, *69*, 58-66.
3. Sun, F.; Sun, Z.; Chen, Q.; Murayama, R.; Nishino, H. Mode conversion behavior of guided wave in a pipe inspection system based on a long waveguide. *Sensors (Basel)* **2016**, *16*.

4. Pei, C.X.; Zhao, S.Q.; Xiao, P.; Chen, Z.M. A modified meander-line-coil EMAT design for signal amplitude enhancement. *Sensor Actuat a-Phys* **2016**, *247*, 539-546.
5. Kang, L.; Zhang, C.; Dixon, S.; Zhao, H.; Hill, S.; Liu, M.H. Enhancement of ultrasonic signal using a new design of rayleigh-wave electromagnetic acoustic transducer. *NDT&E Int* **2017**, *86*, 36-43.
6. Dhayalan, R.; Murthy, V.S.N.; Krishnamurthy, C.V.; Balasubramaniam, K. Improving the signal amplitude of meandering coil EMATs by using ribbon soft magnetic flux concentrators (MFC). *Ultrasonics* **2011**, *51*, 675-682.
7. Thring, C.B.; Fan, Y.; Edwards, R.S., Focused rayleigh wave EMAT for characterisation of surface-breaking defects. *NDT&E Int* **2016**, *81*, 20-27.
8. Mirkhani, K.; Chaggares, C.; Masterson, C.; Jastrzebski, M.; Dusatko, T.; Sinclair, A.; Shapoorabadi, R.J.; Konrad, A.; Papini, M. Optimal design of EMAT transmitters. *NDT&E Int* **2004**, *37*, 181-193.
9. Hirao, M.; Ogi, H. *EMATs for science and industry: Noncontacting ultrasonic measurements*. Springer Science & Business Media: 2013.
10. Ribichini, R.; Cegla, F.; Nagy, P.B.; Cawley, P. Experimental and numerical evaluation of electromagnetic acoustic transducer performance on steel materials. *NDT&E Int* **2012**, *45*, 32-38.
11. Jian, X.; Dixon, S.; Grattan, K.T.V.; Edwards, R.S. A model for pulsed rayleigh wave and optimal EMAT design. *Sensor Actuat a-Phys* **2006**, *128*, 296-304.
12. Jian, X.; Dixon, S. Enhancement of emat and eddy current using a ferrite back-plate. Sensor Actuat a-Phys **2007**, 136, 132-136.
13. Feynman, R.P.; Leighton, R.B.; Sands, M. *The feynman lectures on physics, vol. Ii: The new millennium edition: Mainly electromagnetism and matter*. Hachette UK: 2015.
14. McLyman, C.W.T. *Transformer and inductor design handbook*. Marcel Dekker New York, NY, USA: 2004; Vol. 121.
15. Rueter, D.; Morgenstern, T. Ultrasound generation with high power and coil only EMAT concepts. *Ultrasonics* **2014**, *54*, 2141-2150.
16. Seher, M.; Nagy, P.B. On the separation of lorentz and magnetization forces in the transduction mechanism of electromagnetic acoustic transducers (EMATs). *Ndt&E Int* **2016**, *84*, 1-10.
17. Y, F. The analysis of surface defects using the ultrasonic rayleigh surface wave. University of Warwick, 2008.
18. Guan, W.; Qian, H.; Fang, F.; Luo, Y.; Yang, J.; Chen, B.; Gao, Y.; Muramatsu, K. Numerical modeling of excess loss in sife sheet considering pinning effect. *IEEE Transactions on Applied Superconductivity* **2016**, *26*, 1-4.
19. Kang, L.; Dixon, S.; Wang, K.C.; Dai, J.M. Enhancement of signal amplitude of surface wave EMATs based on 3-d simulation analysis and orthogonal test method. *Ndt&E Int* **2013**, *59*, 11-17.
20. Seher, M.; Challis, R.; Isla, J.; Cegla, F. The effect of metal load material and impedance matching on EMAT performance. *Insight* **2016**, *58*, 536-543.
21. Hao, K.S.; Huang, S.L.; Zhao, W.; Wang, S.; Dong, J.R. Analytical modelling and calculation of pulsed magnetic field and input impedance for EMATs with planar spiral coils. *Ndt&E Int* **2011**, *44*, 274-280.

22. Dhayalan, R.; Balasubramaniam, K. A hybrid finite element model for simulation of electromagnetic acoustic transducer (EMAT) based plate waves. *Ndt&E Int* **2010**, *43*, 519-526.
23. Seher, M.; Huthwaite, P.; Lowe, M.J.S.; Nagy, P.B. Model-based design of low frequency lamb wave EMATs for mode selectivity. *Journal of Nondestructive Evaluation* **2015**, *34*.
24. Rose, J.L. *Ultrasonic waves in solid media*. Cambridge University Press: 1999; p 1807-1808.
25. Dixon, S.; Palmer, S.B. Wideband low frequency generation and detection of lamb and rayleigh waves using electromagnetic acoustic transducers (EMATs). *Ultrasonics* **2004**, *42*, 1129-1136.
26. He, J.; Dixon, S.; Hill, S.; Xu, K. A new electromagnetic acoustic transducer design for generating and receiving s0 lamb waves in ferromagnetic steel plate. *Sensors (Basel)* **2017**, *17*.
27. Bowler, N. Frequency-dependence of relative permeability in steel. *Review of Progress in Quantitative Nondestructive Evaluation, Vols 25A and 25B* **2006**, *820*, 1269-1276.
28. Lakshman, A.; Rao, P.S.V.S.; Rao, K.H. Frequency dependence of initial permeability and magnetic loss factor of in3+ and cr3+ substituted mg-mn ferrites. *Journal of Magnetism and Magnetic Materials* **2004**, *283*, 329-334.
29. Vértesy, G.; Magni, A. Frequency dependence of coercive properties. *Journal of magnetism and magnetic materials* **2003**, *265*, 7-12.
30. Jian, X.; Dixon, S.; Edwards, R.S.; Reed, J. Coupling mechanism of electromagnetic acoustical transducers for ultrasonic generation. *Journal of the Acoustical Society of America* **2006**, *119*, 2693-2701.
31. Isla, J.; Cegla, F. Optimization of the bias magnetic field of shear wave emats. Ieee T Ultrason Ferr **2016**, 63, 1148-1160.